nature catalysis

Article

https://doi.org/10.1038/s41929-024-01190-9

The solvation environment of molecularly dispersed cobalt phthalocyanine determines methanol selectivity during electrocatalytic CO_2 reduction

Received: 29 August 2023

Accepted: 10 June 2024

Published online: 08 July 2024

Check for updates

Quansong Zhu[1,5], Conor L. Rooney[2,5], Hadar Shema[3,5], Christina Zeng[4,5], Julien A. Panetier[4] ✉, Elad Gross[3] ✉, Hailiang Wang[2] ✉ & L. Robert Baker[1] ✉

Heterogenized molecular electrocatalysts are a promising group of materials that can electrocatalytically convert waste molecules into higher-value products. However, how the dispersion state of molecules affects the catalytic process is not well understood. Using cobalt phthalocyanine (CoPc) dispersed on carbon nanotubes (CNTs) as a model system, here we show that increasing the direct interaction of the molecular catalyst with cations notably enhances the CO_2 reduction reaction. Specifically, molecularly dispersed CoPc on CNTs yields an eightfold increase in methanol selectivity compared with aggregated CoPc on CNTs. In situ spectroscopic studies confirm the presence of two intermediates located at different positions of the double layer. Density functional theory calculations further reveal that CoPc molecules inside the Stern layer are active for methanol production due to the direct interaction with cations. Similar enhancement effects are also observed for other reactions, showing that dispersing molecular catalysts into monomeric states is a general design parameter.

Electrochemical conversion of Earth-abundant molecules (for example, H_2O, CO_2 and NO_3^-) is a promising strategy for creating sustainable chemicals and fuels. However, many desirable transformations suffer from slow kinetics and poor selectivity, which demand the development of electrocatalysts to activate the reactants and steer the reaction pathway. Molecular catalysts are desirable due to their well-defined active sites, which can be tuned using structure–activity relationships. Unfortunately, molecular catalysts are typically insulating in the solid state, leading to slow electron transfer from the current collector to the active site when heterogenized on the electrode surface[1,2]. To circumvent this issue, molecular dispersion onto conductive supports enables strong electronic coupling to the catalyst. Molecularly dispersed electrocatalysts comprising metal phthalocyanines or porphyrins supported on graphitic carbon substrates have demonstrated impressive catalytic activity for various small-molecule transformations, including CO_2 electroreduction[3–5], O_2 electroreduction[6,7] and NO_3^- electroreduction[8,9].

Cobalt phthalocyanine (CoPc) adsorbed on carbon electrodes was initially shown to reduce CO_2 to CO by Lieber and Lewis in 1984[10]. They discovered a turnover frequency for CO production from heterogeneous CoPc that was three orders of magnitude larger compared with that of the homogeneous system. In 2017, Liang, Wang and co-workers[11]

[1]Department of Chemistry and Biochemistry, The Ohio State University, Columbus, OH, USA. [2]Department of Chemistry and Energy Sciences Institute, Yale University, West Haven, CT, USA. [3]Institute of Chemistry and Center for Nanoscience and Nanotechnology, Hebrew University, Jerusalem, Israel. [4]Department of Chemistry, State University of New York at Binghamton, Binghamton, NY, USA. [5]These authors contributed equally: Quansong Zhu, Conor L. Rooney, Hadar Shema, Christina Zeng. ✉e-mail: panetier@binghamton.edu; elad.gross@mail.huji.ac.il; hailiang.wang@yale.edu; baker.2364@osu.edu

reported CoPc molecules highly dispersed on carbon nanotubes (CNTs) showing >95% Faradaic efficiency for CO_2 reduction to CO and a current density >50 times higher than that of CoPc directly deposited on carbon electrodes. The follow-up work employing gas diffusion electrodes and/or flow cells further increased the CO production current density[12]. Recently, Liang and co-workers[5] discovered that a similar molecular complex, NiPc, can achieve ~98% selectivity to CO at ~120 mA cm^{-2} once it is dispersed on CNTs—a notable improvement in selectivity and reactivity compared with ~16% for NiPc aggregates at ~5 mA cm^{-2}. However, the reason for the enhancement induced by dispersion is not fully understood. We recently discovered that the CoPc/CNT hybrid unlocks an additional reaction pathway that is not accessed by aggregated or homogeneous forms of CoPc, activating it for the six-electron reduction of CO_2 to methanol (MeOH)[13]. The origin of this unique reactivity warrants further study. The CNT support enables molecular-level dispersion of the molecules, therefore yielding various active sites and a high fraction of electroactive molecules. In addition, the electronic interaction between the graphitic carbon and the molecular complex could also play a role[3,14–16]. Previous mechanistic studies investigating electrocatalytic CO_2 reduction by CoPc using in situ spectroscopy have focused on CO production[17–24]. Studies of the MeOH production mechanism have mostly remained at the theoretical calculation stage[25,26]. Most recently, Ren et al.[27] utilized Fourier-transform infrared spectroscopy and Raman spectroscopy to investigate CO reduction to MeOH by CoPc complexes anchored to multi-walled carbon nanotubes. However, they focused on understanding why CO can be reduced to MeOH but CO_2 cannot. The mechanistic insight into understanding CoPc with different dispersion states, which could have a broader impact on other molecular catalysts and reactions, is still lacking and requires more effort.

In this work, we use kinetic and spectroscopic methods to identify different active sites present in CoPc-based electrocatalysts that exist in distinct solvation environments. This work sheds light on the mechanism for MeOH production from molecularly dispersed CoPc on CNTs and the reason why aggregated CoPc is not active for the reaction. More specifically, with the help of atomic force microscopy (AFM)-based infrared spectroscopy (AFM-IR)[28,29] and surface-selective sum frequency generation (SFG) spectroscopy, we directly identify the presence of CoPc monomers and aggregates, as well as the corresponding adsorbed CO intermediates with and without cation stabilization. We discover that the position of CoPc relative to the electrochemical double layer determines the local solvation structure of the adsorbed reaction intermediates, which affects the stabilization induced by cation coordination, leading to different products. This experimental verification highlights the importance of strategic immobilization of molecular catalysts. The well-dispersed molecular catalyst not only exhibits a higher catalytic turnover rate, but also better selectivity to more reduced products.

Results

Catalytic performance of CoPc catalysts

Three types of CoPc-based electrocatalysts were evaluated: CoPc aggregates (CoPc directly drop-cast onto the carbon paper substrate); a CoPc/CNT hybrid (CoPc molecularly dispersed on CNTs); and a CoPc/CNT mixture (CoPc and CNTs prepared under a solvent environment in which the molecules remain in clusters). For electrochemical measurements, the catalyst loading was controlled such that the number of CoPc molecules on the working electrode was the same across the three materials. This is expected to result in higher activity by the CoPc/CNT hybrid catalyst due to better dispersion, increased accessibility of reactants to the molecular active site and higher conductivity; however, dispersion also has a remarkable effect on selectivity via the formation of unique reaction intermediates, as described below. This can be seen in potential-dependent electrochemical CO_2 reduction in aqueous CO_2-saturated 0.1 M $KHCO_3$, for which notable differences in reactivity are observed between the three materials. CoPc aggregates and the CoPc/CNT mixture show a similar selectivity trend with respect to CO production and H_2 evolution (all potentials in the following contexts are referred relative to the reversible hydrogen electrode (RHE) scale) and then the selectivity decreases at more negative potentials due to the competitive hydrogen evolution reaction (Fig. 1a,c). The CoPc/CNT mixture gives a higher current density relative to CoPc aggregates, which might be attributed to the conductive CNT matrix facilitating the transfer of electrons to CoPc clusters. In addition, the CoPc/CNT mixture produces small amounts of MeOH (<5% Faradaic efficiency). In contrast with the CoPc aggregates and CoPc/CNT mixture, the CoPc/CNT hybrid possesses unique catalytic activity for electrochemical CO_2 reduction, specifically as the potential is scanned from −0.80 to −0.95 V, where we observe increasing selectivity for MeOH to an optimal Faradaic efficiency of 42% and a partial current density of 12 mA cm^{-2} (Fig. 1b), consistent with our previously reported results[13]. Despite the hybrid and mixture catalysts having identical compositions (multi-walled CNTs with 3 wt% CoPc), the rate of MeOH production by the CoPc/CNT hybrid is over 30 times greater than that observed with the CoPc/CNT mixture catalyst. This result indicates that the molecular environment around the CoPc/CNT hybrid active site may be critical towards activating the catalyst for the electroreduction of CO to MeOH. We also performed another control experiment using a low-loading CoPc/CNT hybrid to ensure the same number of electroactive sites as for the CoPc/CNT mixture, which also showed a much higher MeOH selectivity (Supplementary Figs. 2 and 3), indicating that the notable difference in catalytic reactivity is not caused by the number of electroactive sites. Regarding the stability of the CoPc/CNT hybrid catalyst, the methanol selectivity starts to decay within the first 3 h of operation (Supplementary Fig. 4a). However, since it shows good stability for the timescale of SFG measurements (a few minutes), this deactivation does not affect the mechanistic analysis. Based on the design parameters, we prepared another analogue of this catalyst—the CoPc–NH_2/CNT hybrid—which shows better long-term methanol selectivity for 45 h without noticeable decay (Supplementary Fig. 4b). As discussed in more detail later, thorough kinetics, SFG, microscopic and density functional theory (DFT) studies were performed to prove that the CoPc–NH_2/CNT hybrid behaves very similarly to the CoPc/CNT hybrid, having similar dispersion and operating under the same reaction mechanism, indicating that they are almost identical on the several-hour time frame for which all in situ characterizations were performed. Although understanding the difference in stability and further improving CoPc catalyst stability is an important consideration, it is beyond the scope of this current study, which focuses on demonstrating how the dispersion state dictates the catalytic activity of heterogeneous molecular catalysts by controlling the catalyst's local solvation environment. The three CoPc-based electrocatalysts were also evaluated for the electrochemical nitrate reduction reaction (NO_3RR) and oxygen reduction reaction (ORR) to determine whether the observed reactivity trend for the CO_2 reduction reaction (CO_2RR) holds true for other small-molecule reductions. Our results show that this effect extends to additional reactions, with the CoPc/CNT hybrid being far more active for the NO_3RR compared with the other two CoPc-based catalysts, both in terms of rate and Faradaic efficiency for NH_3 production (Fig. 1d,e). The CoPc/CNT hybrid also outperforms the others in catalysing the ORR (Fig. 1f). The proficiency of the CoPc/CNT hybrid catalyst in accomplishing multi-electron reductions with higher rate and selectivity compared with other CoPc-based electrocatalysts is most notable in the context of the CO_2RR, but also generalizable to other electrochemical reactions; however, the origin of this enhanced activity remains unclear.

Characterization of molecular dispersion

For heterogeneous molecular catalytic systems, it is essential to understand how the molecular catalysts are dispersed on the supports.

https://doi.org/10.1038/s41929-024-01190-9

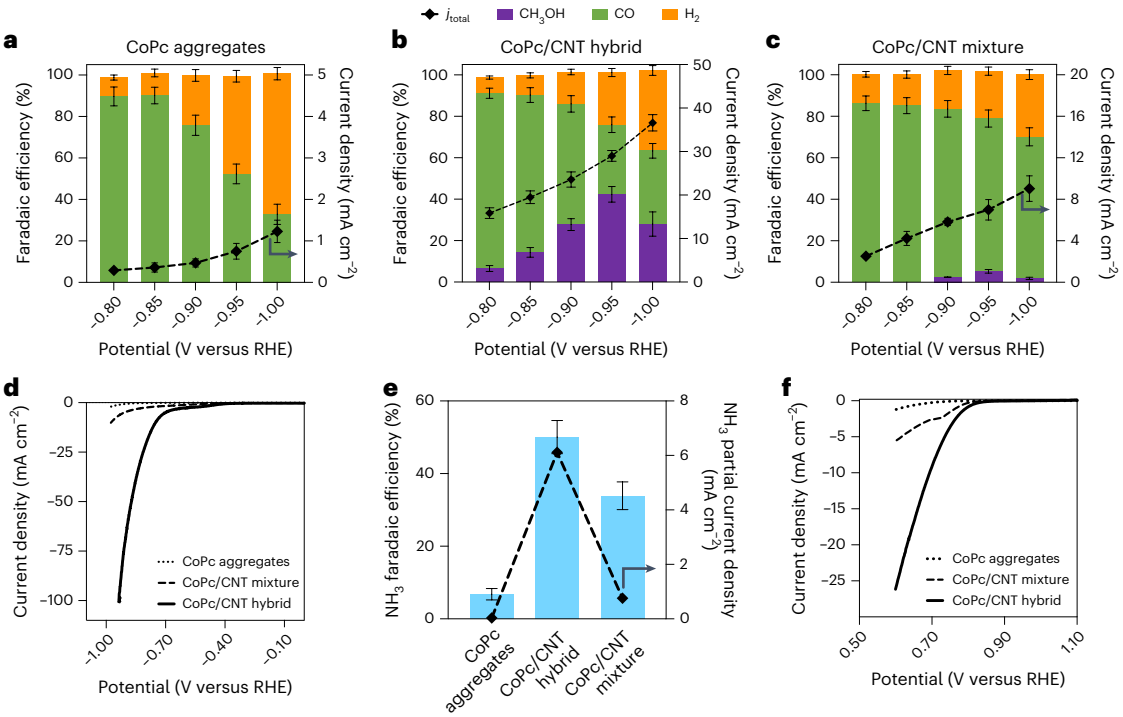

Fig. 1 | Electrocatalytic performance of differently dispersed CoPc electrodes. a–**c**, Potential-dependent CO_2 reduction performance of CoPc aggregates (**a**), the CoPc/CNT hybrid (**b**) and the CoPc/CNT mixture (**c**) in CO_2-saturated 0.1 M $KHCO_3$ electrolyte. Controlled potential electrolysis with isotope-labelled $^{13}CO_2$ confirmed that the produced methanol came from electrochemical CO_2 reduction (Supplementary Fig. 1). **d**,**e**, NO_3^- reduction activity measured by linear sweep voltammetry at 10 mV s^{-1} (**d**) and ammonia production from electrolysis at −0.8 V versus the RHE in Ar-saturated phosphate-buffered (pH 7.2) 0.1 M KNO_3 electrolyte (**e**). **f**, Oxygen reduction activity measured by linear sweep voltammetry at 10 mV s^{-1} in O_2-saturated 0.1 M KOH electrolyte. The results in **a**–**c** and **e** were obtained from three parallel experiments and the data are presented as means ± s.d.

Nanoscale chemical analysis of CoPc distribution on CNTs was performed using AFM-IR measurements. Amine-functionalized CoPc (CoPc–NH_2) was utilized for these AFM-IR measurements due to the noticeable N–H signal. CoPc–NH_2/CNT catalysts were prepared in the same way as CoPc/CNT catalysts except for the presence of the additional amine group, and this hybrid system showed similar catalytic reactivity towards CO_2 electroreduction to that of the CoPc/CNT hybrid without the amine group (Supplementary Fig. 5). As discussed in more detail below, the SFG spectra, calculated reaction profile and adsorbed CO frequencies were very close for CoPc–NH_2 and CoPc, indicating that the amine group does not change the reaction mechanism. Thus, CoPc–NH_2 could serve as a spectroscopically marked equivalent molecule for AFM-IR study. Scanning electron microscopy and transmission electron microscopy measurements were also performed and confirmed that the surface density and dispersion of CoPc were not modified following the addition of an amine functional group (Supplementary Figs. 9–11). Aggregates of CoPc clusters could clearly be seen for the mixture catalyst, whereas no obvious aggregates were observed for the hybrid catalyst. These microscopic measurements further prove the homogeneous distribution of CoPc in the hybrid catalyst and the heterogeneous pattern of the mixture catalyst.

Before AFM-IR measurement, attenuated total reflectance-based infrared spectroscopy measurements were first performed to obtain the reporter's vibrational frequency. The N–H bending mode was probed for CoPc–NH_2 aggregates at 1,606 cm^{-1}, whereas the same mode was probed at 1,632 cm^{-1} for the CoPc–NH_2/CNT hybrid and CoPc–NH_2/CNT mixture (Supplementary Fig. 12). The changes in the vibrational spectrum, induced by CoPc–NH_2 deposition on CNT, are attributed to π–π interactions between the CNTs and the aromatic rings of the Pc ligand. These interactions induce stronger hydrogen bonds of the amine group[30], resulting in a blue shift in the N–H bending mode[31]. For AFM-IR measurements, CoPc–NH_2 aggregates, the CoPc–NH_2/CNT hybrid and the CoPc–NH_2/CNT mixture were deposited on Au films. The height of CoPc–NH_2 aggregates was up to 700 nm (Fig. 2a), which was much greater than that of the other two catalysts. The CoPc–NH_2/CNT hybrid was characterized with a varied height of 5–15 nm with respect to the substrate (Fig. 2b), which is higher than that of bare CNTs that are characterized with an average height of 7 ± 3 nm (Supplementary Fig. 13) and indicates that the CNTs were coated with CoPc. A more heterogeneous height pattern was detected for the CoPc–NH_2/CNT mixture, which was characterized with an average height of 10 ± 2 nm along the CNT and an average height of 15 ± 2 nm near the tips (Fig. 2c). This height pattern was indicative for the CoPc–NH_2/CNT mixture and was not detected for the CoPc–NH_2/CNT hybrid, revealing the more aggregated nature of CoPc in the mixture catalyst. Topography analysis was also conducted for CoPc/CNT catalysts, further emphasizing varied topography for both catalysts. Yet, a more heterogeneous height pattern was observed for the CoPc/CNT mixture (Supplementary Fig. 14).

Infrared mapping at wavenumbers according to peaks observed in the attenuated total reflectance spectra are depicted in Fig. 2d–f. The signal threshold was determined according to the bare CNT signal acquired with the same AFM tip under identical conditions (Supplementary Fig. 13). Infrared mapping of the CoPc–NH_2/CNT hybrid showed a continuous signal across the CNT. A correlation was detected between the topography and infrared maps and enhanced signal was detected on higher areas across the CNT compared with moderate signal on lower areas (Fig. 2e). Infrared mapping of the CoPc–NH_2/CNT mixture showed a different pattern than the one detected for the CoPc–NH_2/CNT hybrid, where the physical mixture displayed a heterogeneous infrared signal that included disconnected islands with strong infrared signal, whereas most of the CNT area was characterized by low or no infrared signal (Fig. 2f). Additional examples demonstrating the same patterns are provided in Supplementary Fig. 15. The infrared maps clearly demonstrate a more homogeneous

https://doi.org/10.1038/s41929-024-01190-9

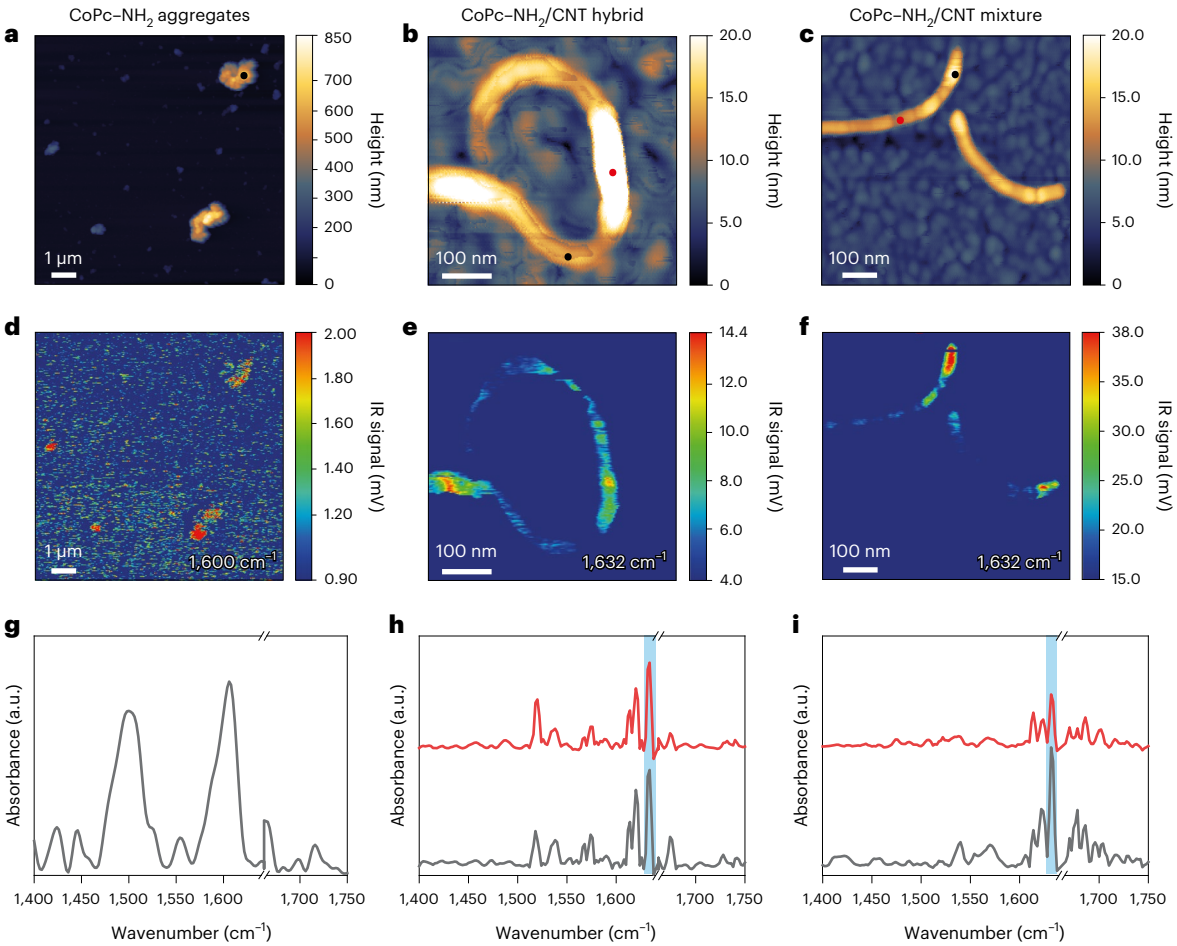

Fig. 2 | AFM-IR measurement of differently dispersed CoPc electrodes. **a**–**c**, AFM topography scans of CoPc–NH_2 aggregates (**a**), the CoPc–NH_2/CNT hybrid (**b**) and the CoPc–NH_2/CNT mixture (**c**). **d**–**f**, Corresponding infrared signal maps at 1,600 cm^{-1} (CoPc–NH_2 aggregates; **d**) and 1,632 cm^{-1} (CoPc–NH_2/CNT hybrid (**e**) and CoPc–NH_2/CNT mixture (**f**)). For the CoPc–NH_2/CNT scans, the signal threshold was equivalent to that of the clean CNT signal intensity acquired by the same AFM probe. **g**–**i**, Local infrared spectra of CoPc–NH_2 aggregates (**g**), the CoPc–NH_2/CNT hybrid (**h**) and the CoPc–NH_2/CNT mixture (**i**) at the locations marked by the coloured dots in **a**–**c**. The location dot colours match those of the spectra they relate to. The break at 1,640–1,665 cm^{-1} is due to laser exchange in that range.

coverage of CoPc–NH_2 on the hybrid structure than the mixture structure. Moreover, the homogeneity of the infrared signal on the CoPc–NH_2/CNT hybrid at lower domains indicates the presence of thin CoPc–NH_2 layers (probably monomers), which do not exist on the CoPc–NH_2/CNT mixture. However, it is clear that in addition to the homogeneous layer of molecularly dispersed CoPc–NH_2 molecules present on the hybrid catalyst, some aggregated clusters also exist, albeit at a lower concentration compared with the CoPc–NH_2/CNT mixture.

More substantial differences in the distribution of CoPc are reflected in the local infrared spectra. Figure 2g shows the localized infrared spectrum acquired from one of the CoPc–NH_2 microparticles (the measurement position is marked by a black circle in Fig. 2a). The infrared spectrum shows two main peaks at 1,500 and 1,606 cm^{-1}, correlated to aromatic C–C stretch and N–H bending, respectively. Infrared spectra were acquired for the CoPc–NH_2/CNT hybrid and three main peaks at 1,632, 1,620 and 1,520 cm^{-1} were detected (Fig. 2h). Detection of the 1,632 cm^{-1} peak occurred on various sites of other hybrid entities as well (Supplementary Fig. 16), indicative of the homogeneous coverage detected in Fig. 2e. The infrared spectrum acquired on a high site of the CoPc–NH_2/CNT mixture showed a similar signal-to-noise level (black spectrum in Fig. 2i). However, the site with barely visible signal at Fig. 2f and lower height in Fig. 2c displayed a poor signal-to-noise ratio (red spectrum in Fig. 2i), demonstrating the heterogeneous coverage in the mixture sample. Overall, these results confirm the presence of molecular aggregates in all three catalysts, whereas molecularly dispersed CoPc molecules exist at a high density only in the CoPc–NH_2/CNT hybrid system.

Different intermediates leading to CO and MeOH

To further investigate the mechanism of enhanced MeOH production from CoPc/CNT hybrid catalysts, plasmon-enhanced SFG vibrational spectroscopy was employed to observe the potential-dependent binding of reaction intermediates during in situ electrocatalysis. As a second-order nonlinear technique, SFG spectroscopy is interface selective, enabling direct detection of reaction intermediates at the catalyst/electrolyte interface[32,33]. By utilizing plasmonic signal enhancement from a gold or silver substrate, we showed previously that the detection limit of this technique is below 1% of a surface monolayer[34], which is sufficient to detect CO_2RR intermediates on CoPc/CNT catalysts with ~3% mass loading. In this work, a plasmonic silver electrode was used as a substrate for the CoPc catalysts. An ultrathin (Al_2O_3; 2.5 nm) film was deposited on the silver substrate by atomic layer deposition before catalyst deposition. This ultrathin passivation layer prevents CO adsorption on silver while still allowing moderate current densities through the CoPc catalysts (Supplementary Figs. 17 and 18). Both the 800 nm and mid-infrared beams were plasmonically coupled to the electrode/electrolyte interface through the silver layer, as described previously[34]. This geometry enables in situ detection of reaction intermediates

https://doi.org/10.1038/s41929-024-01190-9

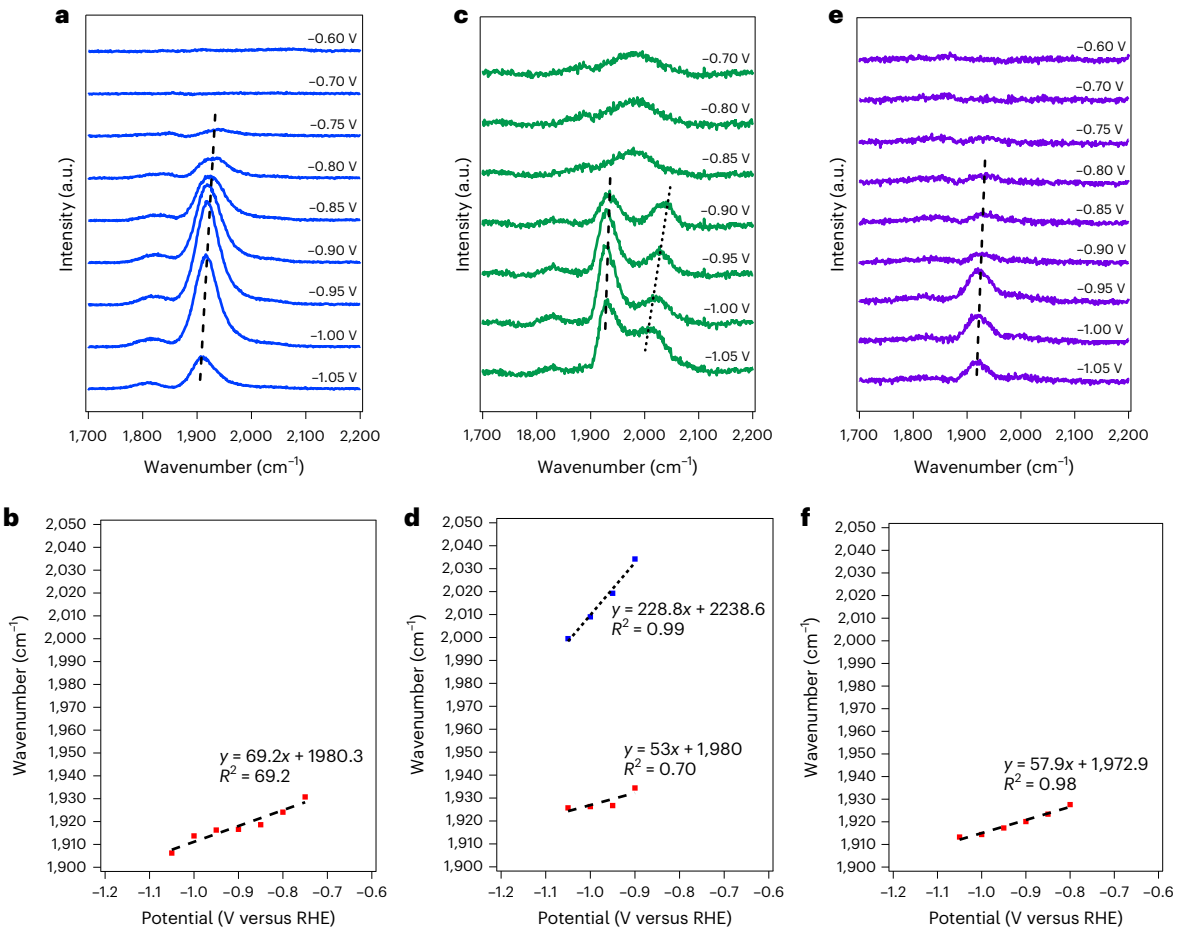

Fig. 3 | SFG measurement of differently dispersed CoPc electrodes. a,**c**,**e**, Potential-dependent SFG spectra of CoPc aggregates (**a**), the CoPc/CNT hybrid (**c**) and the CoPc/CNT mixture (**e**) obtained under in situ conditions. **b**,**d**,**e**, Fitted peak position and Stark tuning behaviour for the corresponding CoPc electrodes: CoPc aggregates (**b**), the CoPc/CNT hybrid (**d**) and the CoPc/CNT mixture (**f**).

during potential-dependent CO_2RR while avoiding mass transport limitations imposed by coupling the beams through an ultrathin electrolyte layer, as is typical for other spectro-electrochemical SFG measurements. As shown in Fig. 3a, a strong peak at ~1,920 cm^{-1} was observed for the CoPc aggregates at the relevant potential range of CO production. The frequency matched previous reports of CO adsorbing to Co[35,36], and the ^{13}C isotopic labelling experiment also showed the expected frequency shift (Supplementary Fig. 19). Thus, we assigned this feature to in situ-generated CO adsorbing to the Co centre of CoPc. A similar feature was also observed for the CoPc/CNT mixture (Fig. 3e), but with weaker intensity, as a result of fewer CoPc molecules being embedded in the CNT mixture. However, for the CoPc/CNT hybrid, a unique feature was observed at ~2,020 cm^{-1} in addition to the common CO feature at 1,920 cm^{-1} (Fig. 3c). This additional feature appeared within a potential window beginning at −0.90 V, which closely matches the potential range at which the MeOH yield becomes notable (see Fig. 1b). The same experiment was also conducted for the amine-functionalized CoPc–NH_2 catalysts and similar spectroscopic patterns were observed (Supplementary Fig. 20). A common CO feature was present for all three catalysts, whereas a second unique feature was only observed for the CoPc–NH_2/CNT hybrid. Since the appearance of this feature was closely correlated with MeOH production, we hypothesize that it may represent an active surface intermediate required for MeOH formation. To verify the identity of this peak, we conducted a ^{13}C isotopic labelling experiment and, as expected, this feature shifted to 1,970 cm^{-1} (Supplementary Fig. 19), indicating that it was also CO. We also performed DFT calculations to prove that the observed features could not be other reaction intermediates during CO_2 reduction (for example, *CHO or *CH_2O), since their calculated frequencies are below 1,800 cm^{-1} (Supplementary Table 1). Thus, we propose that for the CoPc/CNT hybrid there are two types of CO intermediate adsorbing at two different types of site. One intermediate is selective to CO and is consistently present in aggregated CoPc molecules, whereas the other is selective to MeOH and is only present on the dispersed CoPc molecules of the CoPc/CNT hybrid catalyst. We note that we performed careful control experiments showing that there was no interference in these measurements from CO adsorption to either the Ag substrate or the CNT electrode. As shown in Supplementary Fig. 17, SFG measurement for the Al_2O_3-passivated Ag electrode, with and without CNT loading and under both CO_2 and CO purging conditions, showed no sign of CO adsorption. Additionally, the kinetics measurement for the CoPc/CNT hybrid loaded on an Al_2O_3/Ag electrode showed similar MeOH production (Supplementary Fig. 18) to those loaded on carbon paper (Fig. 1), indicating that the Al_2O_3-passivated Ag substrate used for in situ SFG only serves as an electron conductor and does not influence the catalysis.

Two active sites based on unique solvation environments

To further understand the difference between two types of CO intermediate, we conducted a careful investigation into their respective Stark tuning behaviour. Figure 3b,d,f shows the frequency shift of these two species as a function of the applied potential. The common CO intermediate with lower total frequency also shows a smaller Stark tuning slope of only ~60 cm^{-1} V^{-1}, whereas the CO intermediate

https://doi.org/10.1038/s41929-024-01190-9

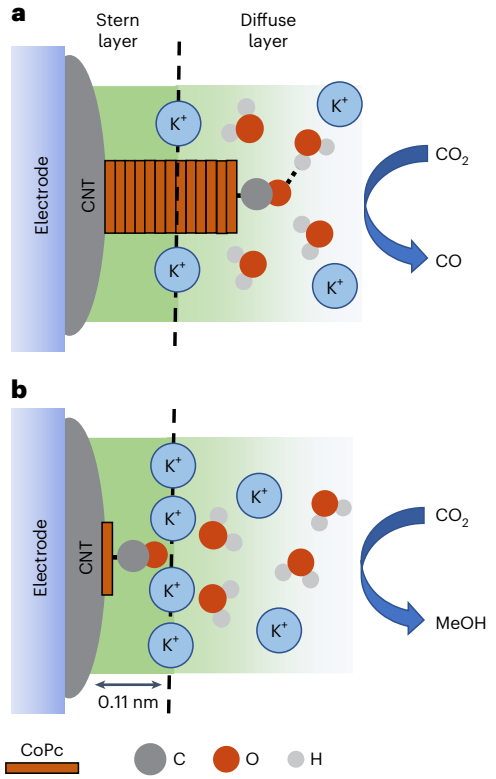

Fig. 4 | Schematics of interfacial structures. a,**b**, Proposed interfacial structures for the CoPc/CNT mixture (**a**) and CoPc/CNT hybrid (**b**). In **a**, CoPc molecules aggregate and extend into the diffuse layer where the adsorbed inactive CO is located. In **b**, the CoPc monomer and adsorbed active CO are located within the Stern layer.

correlated with MeOH production has a higher absolute frequency, as well as a much larger Stark tuning slope of 230 cm^{-1} V^{-1}. This represents a nearly fourfold increase in the Stark tuning slope compared with the common intermediate associated with CO production. Similar results were also observed for the amine-functionalized CoPc–NH_2 catalysts (Supplementary Fig. 20). This substantial increase in the Stark tuning slope indicates that the CO intermediate responsible for MeOH is located in a stronger electric field environment and that the electric field at this site is more sensitive to applied potential compared with the other CO intermediate responsible for CO formation. One possible explanation for this is that the vibration displaying a higher Stark tuning slope represents CO adsorbed to CoPc monomers located inside the electrochemical Stern layer, whereas the CO vibration displaying a lower Stark tuning slope represents CO adsorbed to CoPc aggregates that extend beyond the Stern layer into the diffuse region of the electrical double layer (EDL). The electric field in the diffuse region of the EDL is much weaker than the Stern layer. Based on AFM-IR measurements, CoPc aggregates range in size from several nanometres in the CoPc/CNT mixture to even larger in the CoPc aggregates. In both cases, this would place the exposed CoPc site far outside the Stern layer, which is <1 nm. This explanation is also consistent with the previous observation by Lian's group[37], which showed that a nitrile group also experiences very different frequency shifts based on its location within the EDL, as determined by the distance of the Stark reporter from the electrode surface. Here we note that bulk CoPc solid exhibits low conductivity, as demonstrated in previous studies[38–40]. Thus, it is unlikely that aggregated CoPc in CoPc aggregates and CoPc/CNT mixture would maintain sufficient surface charge to establish a Stern layer. CoPc must be molecularly dispersed to be located within the Stern layer generated by CNT, whereas aggregated CoPc extends into the diffuse layer.

From the Stark tuning slope, it is possible to determine the absolute Stern layer thickness by assuming a given potential drop between the electrode surface and an adsorbed electrolyte cation based on Gouy–Chapman–Stern theory (see Supplementary Notes for calculation details). Here the Stern layer thickness is defined as the distance from the electrode surface to the outer Helmholtz plane. This calculation shows that the Stern layer thickness is 0.11 nm. This closely matches the measured height (0.15 nm) of CO_2 adsorbing to a flat-lying CoPc monomer by in situ electrochemical scanning tunnelling microscopy[41], suggesting that at the site of MeOH formation, an adsorbed cation coordinates directly to the adsorbed intermediate bound to the CoPc catalyst within the Stern layer. As discussed above, the AFM-IR measurement shows that CoPc molecules in the CoPc/CNT hybrid catalyst are uniformly distributed as a thin monolayer directly on the CNT surface, suggesting that CO adsorbed on these Co sites would be located within the Stern layer where it can directly coordinate to electrolyte cations. In contrast, heterogeneously distributed CoPc aggregates in the CoPc/CNT mixture lead to CoPc active sites extending far into the diffuse layer where the electric field changes slowly as a function of the applied potential, giving rise to a much smaller Stark tuning slope. Together these observations support the hypothesis that the unique CO intermediate detected only on the CoPc/CNT hybrid catalyst resides within the Stern layer, consistent with adsorption on molecularly dispersed CoPc catalysts on the CNT electrode, and this CO is believed to be in direct coordination with an electrolyte cation. In contrast, the CO intermediate responsible for CO formation is adsorbed on CoPc aggregates far from the CNT, having no direct coordination to electrolyte cations. Below we provide experimental and theoretical evidence showing that the different solvation environments not only explain the observed frequency shift, but these solvation effects are also responsible for controlling the reaction selectivity between CO and MeOH.

Stabilizing the CO intermediate by cation coordination

We now consider the reason why a CO intermediate bound to a CoPc catalyst inside the Stern layer would be more selective for MeOH formation compared with a CO intermediate bound to CoPc in the diffuse layer. To begin, we show that the frequency shift between these two CO intermediates reflects the unique solvation environments, where CO in the diffuse layer is frequency shifted due to hydrogen (H) bonding with the electrolyte, whereas CO residing inside the Stern layer is shielded from H bonding by direct coordination with the cation[42]. To explain, the blue shift of active CO relative to the inactive CO can be attributed to the H-bonding effect as a result of a unique local solvation environment within the Stern layer. Franzen[43] discovered that the frequency of CO adsorbing to a myoglobin molecule (Fe–N_4), which is very similar to Co–N_4 in CoPc, shifts from 2,020 cm^{-1} in a non-H-bonding environment such as CH_4 to 2,000 cm^{-1} in a weak H-bonding environment such as NH_3 and to 1,970 cm^{-1} in a strong H-bonding environment[43]. This frequency shifts for non-H-bonded and H-bonded CO closely match those observed here for the CO intermediate located inside and outside the Stern layer, respectively. To further evaluate this explanation, we also performed DFT calculations for the C–O bond vibrational stretching mode of the monoanionic CoPc–CO, $(\mathbf{11})^{-}\nu_{CO}$, in the presence of varying numbers of explicit water molecules. As shown in Supplementary Tables 2–4, DFT calculations based on several DFT functionals all showed that increasing the number of surrounding water molecules increases red shifts of CO frequency (ν_{CO}). The unscaled ν_{CO} of CoPc–CO (total spin angular momentum (S), $\langle S^2 \rangle = 0$) given by the hybrid version of the Tao, Perdew, Staroverov and Scuseria functional without coordinating water molecules was 1,967 cm^{-1}, and this value decreased to 1,873 cm^{-1} with two water molecules nearby, corresponding well with the experimentally observed $\Delta\nu_{CO}$ due to the presence of water. Combining evidence from in situ SFG spectroscopy and DFT calculations, here we provide a schematic to explain

https://doi.org/10.1038/s41929-024-01190-9

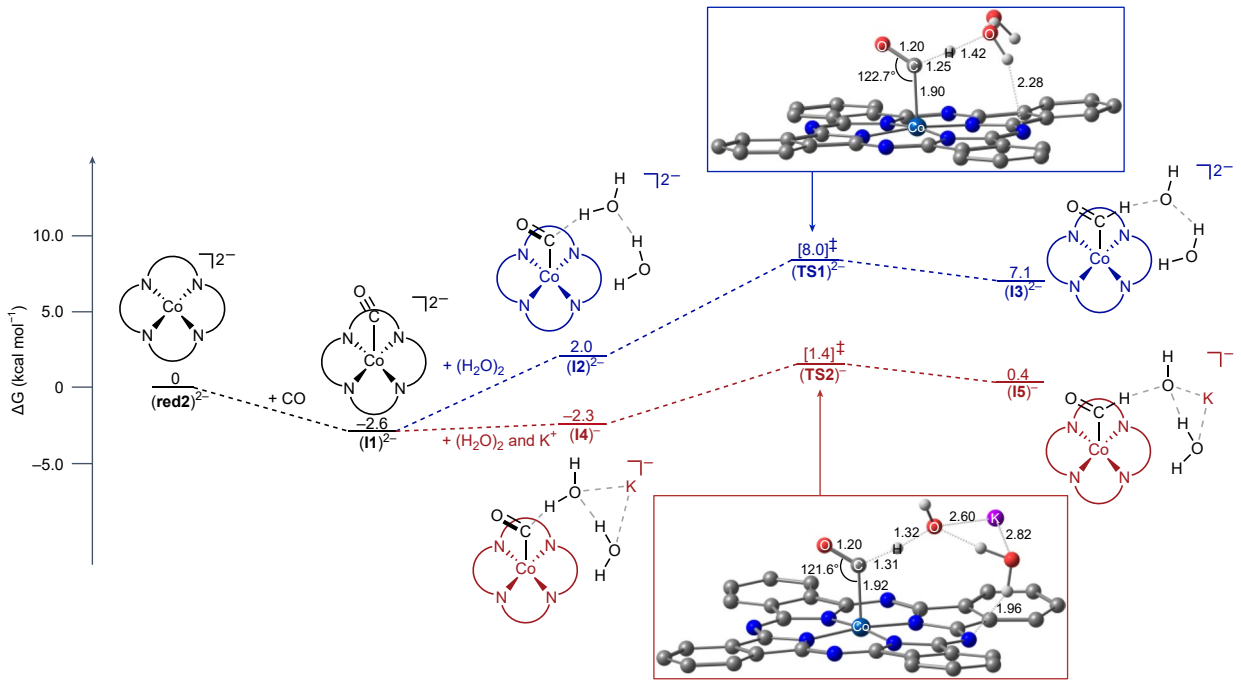

Fig. 5 | DFT calculations of the cation coordination effect. Computed Gibbs-free energy reaction profile of CoPc-catalysed CO protonation via a water dimer (in blue) in the presence of a K^+ cation (in red) yielding a *CHO intermediate. All of the Gibbs-free energies are with respect to the separated reactants and have a doublet ground state. Note that CoPc–CO, $(\mathbf{I1})^{2-}$, features a cobalt(II) centre, which has a lower Gibbs-free energy than the cobalt(I) species by 3.3 kcal mol^{-1} (Supplementary Table 6). The optimized geometry of the transition state $(\mathbf{TS1})^{2-}$ in the presence of a water dimer is shown in the blue box and the optimized geometry of the transition state in the presence of both a water dimer and K^+, $(\mathbf{TS2})^-$, is shown in the red box. Distances are given in angstroms and non-participating hydrogen atoms have been excluded for clarity. The Mulliken spin population is given for cobalt.

the interfacial structure associated with the CoPc/CNT hybrid catalyst and CoPc/CNT mixture catalyst (Fig. 4). For aggregated CoPc catalysts in the CoPc/CNT mixture (Fig. 4a), CoPc molecules aggregate via π stacking interactions and only the exposed CoPc molecule at the top is catalytically active[1,24]. The height of this CoPc aggregate is on the order of a few nanometres, as seen by AFM-IR, extending well into the diffuse layer. Consequently, if CO_2 were reduced to CO at these sites, CO would be H bonded with surrounding water molecules as the concentration of ions would be similar to that of the bulk electrolyte. However, for the CoPc/CNT hybrid catalyst (Fig. 4b), although there could be CoPc aggregates, there are also many molecularly dispersed CoPc molecules supported on the CNT surface. These CoPc active sites are located within the Stern layer. It has been recognized in previous studies that K^+ cations can fully or partially dehydrate in the Stern layer[44–46], as driven by the strong electric field and its small hydration energy. Coordination of the adsorbed CO intermediate with partially desolvated K^+ cations will shield the CO from H bonding to water. This non-H-bonded CO has a higher vibrational frequency and also shows a larger Stark shift compared with the intermediate present on the aggregate catalyst in the diffuse layer. As will be discussed in more detail below, the molecular solvation environment and interaction with cations notably influence the catalytic selectivity to MeOH through intermediate stabilization.

The effect of electrolyte cations on the CoPc-catalysed CO_2RR was further evaluated by DFT calculations (Fig. 5). Starting from a doubly reduced CoPc catalyst, $(\mathbf{red2})^{2-}$, introduction of CO allows for the formation of CoPc–CO $(\mathbf{I1})^{2-}$. Note that $(\mathbf{I1})^{2-}$ has one unpaired electron on cobalt, suggesting a cobalt(II) species, whereas the cobalt(I) compound is 3.3 kcal mol^{-1} higher in energy (Supplementary Table 6). To evaluate whether adsorption is influenced by the molecular solvation environment, we looked at the CO adduct in the presence of a two-water-molecule cluster, $(\mathbf{I2})^{2-}$. In this case, adsorption was 4.6 kcal mol^{-1} more endergonic than for $(\mathbf{I1})^{2-}$ and led to a cobalt(I) compound. It matched the recent spectroscopic characterizations, which identified the active site of CoPc/CNT to be the doubly reduced molecule (that is, a metal-based first reduction involving Co(II) → Co(I) occurring at ~0.1 V versus the RHE and a second ligand-based reduction forming the active CO_2 reduction catalyst $Co(I)Pc^{1-}$)[27,47]. Note that electronic structure calculations using our previously published five-water cluster yielded qualitatively similar results and are shown in Supplementary Fig. 23 (ref. 48). Interestingly, the addition of a K^+ cation to simulate the molecular solvation environment inside the Stern layer lowered the endergonicity of CO adsorption to 0.3 kcal mol^{-1}. More specifically, the cation provided substantial stabilization to the water cluster and adsorbed CO in $(\mathbf{I4})^-$, lowering the energy of the intermediate by 4.3 kcal mol^{-1} relative to that of $(\mathbf{I2})^{2-}$. The rate-determining step for further reduction of CO was the subsequent protonation, which required an activation barrier of 10.6 kcal mol^{-1} with respect to the infinitely separated reactants in the absence of K^+ $(\mathbf{TS1})^{2-}$. In contrast, the activation barrier was lowered to 4.0 kcal mol^{-1} in the presence of K^+ $(\mathbf{TS2})^-$. After CO protonation, K^+ also acts as a counterion for the generated hydroxyl anion in $(\mathbf{I5})^-$, leading to stabilization of the *CHO intermediate by 6.7 kcal mol^{-1} relative to the same *CHO intermediate in the absence of K^+ $(\mathbf{I3})^{2-}$. The resulting formyl species has been proposed to be a key intermediate towards MeOH formation[25,49]. We note here that it has been well established in the literature that the first hydrogenation step (that is, *CO to *CHO) is the rate-determining step during CO_2 reduction to MeOH[25,27,50]. The later steps after *CHO formation are not critical for understanding the mechanism of MeOH formation. Thus, in this work, we focused our calculations and discussion on the early steps until *CHO and we expect that future theoretical work will provide more insights into the later steps. Summarizing the results of these DFT calculations, cation-mediated stabilization of *CO and *CHO intermediates plays a key role in MeOH synthesis. In the Stern layer, water molecules are shielded by cations. These electrolyte cations stabilize CO adsorption to doubly reduced CoPc and lower

https://doi.org/10.1038/s41929-024-01190-9

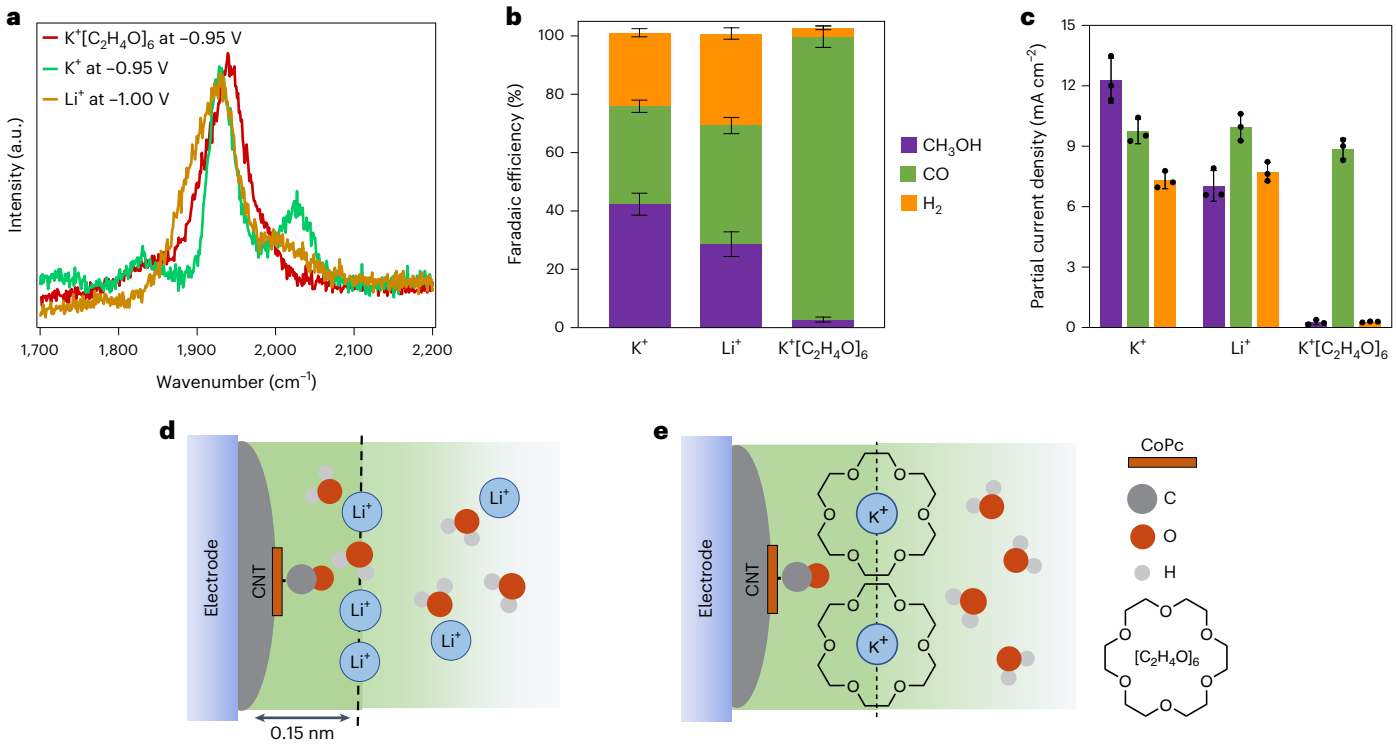

Fig. 6 | SFG spectra, kinetics results and interfacial structures from the cation-dependent study. a, In situ SFG spectra for the CoPc/CNT hybrid in electrolytes containing K^+, Li^+ and crown ether-complexed $K^+[C_2H_4O]_6$. **b**,**c**, Faradaic efficiency (**b**) and partial current density (**c**) to H_2, CO and CH_3OH obtained from electrocatalytic performance measurement in CO_2-saturated 0.1 M $KHCO_3$ (K^+), 0.1 M $LiHCO_3$ (Li^+) or 0.1 M $KHCO_3$ + 0.1 M $[C_2H_4O]_6$ electrolytes ($K^+[C_2H_4O]_6$) at pH 6.8 and under an applied potential of −0.94 V versus the RHE. The results in **b** and **c** were obtained from three parallel experiments and the data are presented as means ± s.d. Data points are included as black dots in **c**. **d**,**e**, Proposed interfacial structure for the CoPc/CNT hybrid in electrolytes containing Li^+ (**d**) or $K^+[C_2H_4O]_6$ (**e**).

the activation barrier for formation of the *CHO intermediate, which serves as a precursor to MeOH production. In contrast, H bonding in the diffuse layer is unable to stabilize *CO and *CHO intermediates, as well as cations, leading to rapid desorption of CO from CoPc aggregates with no possibility for MeOH formation. Unlike heterogeneous catalysts, where active and inactive sites are both located within the Stern layer, molecular catalysts can be tuned by positioning them at different positions with respect to the EDL. Specifically, only CoPc catalysts that are molecularly dispersed onto the CNT electrode inside the Stern layer are capable of CO_2RR to MeOH due to direct interaction with K^+. Although it is possible that they would generate CO as the final product under certain conditions, they are more active than catalysts exhibiting MeOH-inactive sites even when both producing CO. In contrast, CoPc aggregates exhibit MeOH-inactive sites primarily in the diffuse region of the EDL and are selective only for CO formation, thus they are not capable of producing any MeOH.

To further validate the proposed mechanism for cation-mediated MeOH synthesis, which results from the molecular solvation environment at the electrode/electrolyte interface, we performed two additional experiments. The results of both showed that MeOH production is extremely sensitive to the interfacial solvation structure. The first control experiment was to use Li^+ instead of K^+ as the electrolyte cation. Li^+ ($\Delta H_{hydration}$ = −515 kJ mol^{-1}) has a stronger hydration shell compared with K^+ ($\Delta H_{hydration}$ = −322 kJ mol^{-1})[51], so Li^+ will tend not to desolvate upon adsorption to the electrode surface to create the Stern layer. Consequently, we expect a lower MeOH yield for the CoPc/CNT hybrid in Li^+ electrolyte since even the CO intermediate within the Stern layer can now be H bonded with the hydration shell of Li^+, lacking stabilization from direct coordination of *CO to the cation. As shown in Fig. 6a, the SFG spectra of CO in $LiHCO_3$ showed the common CO intermediate with a frequency ~1,920 cm^{-1} and a weak shoulder ~2,000 cm^{-1}. The presence of the shoulder feature indicates that some *CO intermediates are partially shielded from H bonding by Li^+, but these intermediates for MeOH formation are notably reduced in Li^+ compared with K^+ electrolyte. The calculated Stern layer thickness from the Stark tuning of this high-frequency shoulder peak is 0.15 nm (Supplementary Notes), which is also slightly larger than with K^+. The fact that this feature is weaker and red shifted compared with the case of K^+ suggests that Li^+ is partially hydrated at the electrode surface, allowing for H bonding in the Stern layer. Thus, fewer CO molecules can be stabilized by coordinating with Li^+ compared with K^+, as shown by the schematic in Fig. 6d. Comparing the kinetics of MeOH formation in Li^+ and K^+ electrolytes, the Faradaic efficiency for MeOH in Li^+ electrolyte decreases by 33% and the total yield decreases by 43% compared with the K^+ electrolyte, as shown in Fig. 6b,c. Both the SFG spectra and kinetic results match predictions (that is, increasing the extent of H bonding and decreasing the cation stabilization of *CO and *CHO hinders MeOH production).

In the second control experiment, we evaluated whether it is possible to completely eliminate MeOH production from the CoPc/CNT hybrid catalyst by blocking direct coordination of the K^+ cation to *CO and *CHO using a crown ether. Crown ether is known to chelate the cation in solution and block its interaction with other species[52,53]. Here we used 18-Crown-6, whose hole size fits the K^+ cation, forming a stable K^+–18-Crown-6 complex[54,55]. In this case, only the common CO intermediate responsible for CO production was observed by SFG, whereas the more selective CO intermediate at high frequency was completely absent (full spectra as a function of applied potential are shown in Supplementary Fig. 26). Additionally, the kinetic measurements showed that there was almost no MeOH production in the

presence of the crown ether (Fig. 6b,c), confirming that without direct interaction of *CO with K^+ MeOH formation is not possible, even on the molecularly dispersed CoPc catalyst. Furthermore, the hydrogen evolution reaction was also suppressed by the crown ether, indicating very limited water present at the interface. Thus, we propose the interfacial structure as depicted in Fig. 6e. 18-Crown-6 blocks the interaction between the K^+ and CO intermediate, which completely suppresses MeOH production. This also explains the disappearance of the active CO intermediate in SFG spectra. The active CO intermediate is unstable without cation coordination and consequently it desorbs quickly from the CoPc catalyst and is not detectable by SFG.

Both of these control experiments support the proposed mechanism. Namely, the distinct local solvation environment for molecularly dispersed CoPc induces direct cation coordination with the reaction intermediate, which stabilizes CO adsorption and enables further reduction to MeOH via a *CHO intermediate. By changing the solvation structure with different cations or chelating cations with crown ether it is possible to influence the MeOH selectivity and yield, confirming that this reaction pathway is extremely sensitive to cation coordination and solvation structure inside the Stern layer of the molecularly dispersed catalyst.

Conclusions

In summary, this work shows that molecularly dispersed CoPc on CNTs (that is, the CoPc/CNT hybrid) produces a substantial amount of MeOH, whereas CoPc aggregates or CoPc/CNT mixture produce only CO. AFM-IR measurements showed the presence of CoPc aggregates in both the hybrid and the mixture, whereas a molecularly dispersed thin layer of CoPc was observed only for the CoPc/CNT hybrid catalysts. Thus, a clear correlation between the dispersion state and catalytic performance of CoPc can be drawn where molecularly dispersed CoPc on CNTs displays notably enhanced selectivity to MeOH whereas aggregated CoPc produces primarily CO. We further employed the in situ SFG technique to understand the mechanism for MeOH synthesis by molecularly dispersed CoPc catalysts. The results showed that two types of CO species with different frequencies and Stark tuning behaviour are present on CoPc/CNT hybrid catalysts. One of these represents CO adsorbed on CoPc aggregates, where CO exists in the diffuse layer and is H bonded with the aqueous electrolyte. The other represents CO adsorbed on molecularly dispersed CoPc, where CO exists in the Stern layer and is directly stabilized by interaction with K^+ cations. On the basis of DFT calculations, a mechanism is proposed where CO intermediates adsorbing to molecularly dispersed CoPc located within the Stern layer experience direct interaction with alkali cations, which stabilize *CO and notably lower the barrier for the formation of MeOH through a *CHO intermediate. In contrast, CO intermediates adsorbing to CoPc aggregates are located outside the Stern layer, where they are not stabilized by cation interactions and desorb before protonation. This mechanism is consistent with the observation that replacing K^+ with Li^+ or chelating K^+ using a crown ether suppresses MeOH formation.

This work highlights the important effect of molecular solvation structure and cation coordination on the activity and selectivity of electrochemical CO_2 conversion. In addition to the CO_2RR, similar effects were also observed for the NO_3RR and ORR. Unlike purely heterogeneous electrocatalysts, where all surface sites reside inside of the Stern layer, correct positioning of molecular catalysts relative to the EDL represents a critical design parameter for heterogenizing molecular electrocatalysts that has been largely overlooked. Because molecular aggregation can occur easily, this aspect of catalyst design is required to access enhancement effects resulting from direct cation coordination and the unique solvation structure only present inside the Stern layer. Together, this work shows that dispersion of molecular catalysts on a supporting electrode is as critical for catalyst optimization as the synthetic design of the molecular catalyst, where precise positioning of the molecular catalyst with respect to the EDL is a key parameter for efficient CO_2 conversion to MeOH via a cation-assisted reaction mechanism. This lesson is also applicable to other molecular catalytic systems and here we recommend that the field pays substantial attention to it in future work.

Methods

Electrode preparation

The synthesis of CoPc–NH_2, purification of as-received multi-walled CNTs (FT9100; Cnano) and loading of CoPc and CoPc–NH_2 onto purified CNTs to prepare the hybrid catalysts were all carried out as detailed in our previous work[13]. Briefly, 30 mg CNTs were dispersed in 30 ml *N*,*N*-dimethylformamide (DMF) and sonicated for 30 min. Then, 1.5 mg CoPc (or CoPc–NH_2) dissolved in 15 ml DMF was added to the CNT suspension. The mixture was sonicated for 30 min before stirring for 20 h. Subsequently, the mixture was centrifuged and the precipitate was washed with DMF and ethanol. Finally, the precipitate was lyophilized to yield the final hybrid catalyst. To prepare the CoPc/CNT and CoPc–NH_2/CNT mixture catalysts, the same procedure was followed as for the hybrid catalysts except ethanol was used instead of DMF and the amount of CoPc (or CoPc–NH_2) was changed to 1 mg. The weight percentage of CoPc and CoPc–NH_2 in their respective CNT hybrid and mixture catalysts was 3.2%, as measured by inductively coupled plasma mass spectrometry. Catalyst ink was prepared by dispersing 2 mg hybrid or mixture catalyst in 2 ml ethanol with 6 µl 5 wt% Nafion solution and sonicating for 1 h. Once well dispersed, 4 × 50 µl catalyst ink was drop-cast onto a 0.5 cm^2 section of a 0.5 cm × 2.5 cm piece of carbon fibre paper (Toray 030) and dried under an infrared lamp. The prepared working electrodes had a catalyst-covered geometric area of 0.5 cm^2 and a catalyst mass loading of 0.4 mg cm^{-2}. The CoPc or CoPc–NH_2 aggregate electrodes were prepared via a similar procedure except the drop-casting dispersion was 0.2 mg ml^{-1} concentration and the total volume drop-cast was 32 µl. As described above, all catalyst electrodes were prepared with the same CoPc (or CoPc–NH_2) mass loading of 13 µg cm^{-2}.

Electrolyte purification measurements

Purification of aqueous electrolyte solutions (500 ml) was conducted with a two-electrode setup using two 99.99% Ti foil electrodes (10 cm × 5 cm). The purification was conducted with stirring at 2.5 V until the current decreased to 150 µA. The current was then maintained at 150 µA for 24 h. At the end of the purification, the Ti electrodes were removed from the solution before the applied potential was released to avoid the electrodeposited impurities from re-entering the solution.

Electrochemical measurements

Electrochemical measurements were carried out using a BioLogic VMP3 Potentiostat and a custom-made gas-tight two-compartment H-cell. The anodic and cathodic compartments were separated by an anion exchange membrane (Selemion DSV). Each compartment contained 12 ml electrolyte and 18 ml gas headspace. A graphite rod was used as the counter electrode and placed in the anodic compartment. The reference electrode was Ag/AgCl (saturated KCl) and this was placed in the cathodic compartment near the working electrode. The cathodic compartment included two tubing ports: the in-tubing was placed in the electrolyte and connected to a flowmeter, whereas the out-tubing was placed in the headspace and connected to the gas chromatograph. Gas flowed continuously at a rate of 20 standard cubic centimetres per minute. The ohmic drop between the working electrode and reference electrode was determined using potentiostatic electrochemical impedance spectroscopy at −0.5 V versus Ag/AgCl between 200 kHz and 1 Hz with an amplitude of 10 mV. The resistance (R) was determined as the intersection of the curve with the real axis of the Nyquist plot and the current (i) is given by the potentiostat. The internal resistance was then corrected during all of the electrolysis experiments with 100% iR

compensation, which is the voltage loss caused by the electrolyte solution between the working electrode and reference electrode. Current densities were calculated with respect to the catalyst-covered geometric area of the working electrode. All of the potentials were converted to the RHE scale using the following equation: $V_{RHE} = V_{Ag/AgCl} + (0.1976\ V) + (0.0592\ V) \times pH$. For the CO_2 reduction experiments, unless otherwise stated, the electrolyte was 0.1 M aqueous $MHCO_3$ (where M = Li or K). Before the start of each electrolysis the electrolyte was pre-saturated with CO_2 (or Ar for the control experiments) by bubbling for at least 20 min. For the cation dependence study, a stoichiometric amount of 18-Crown-6 (>99%; Sigma–Aldrich) was added to the 0.1 M $KHCO_3$ electrolyte. Controlled potential electrolysis was for a 30 min duration and the mean from three independent measurements was reported. For the NO_3^- reduction experiments, the electrolyte was 0.1 M aqueous phosphate buffer (pH 7.2) with 0.1 M KNO_3. The electrolyte was pre-saturated with Ar by bubbling for at least 20 min before the measurement. Controlled potential electrolysis was performed for 30 min duration. For the O_2 reduction experiments, the electrolyte was 0.1 M aqueous KOH. The electrolyte was pre-saturated with Ar by bubbling for at least 20 min before the measurement. To increase mass transport of the reactant gas to the catalyst, the in-tubing was placed directly next to the backside of the working electrode.

Product quantification

The gas products (H_2 and CO) of electrocatalysis were analysed using a gas chromatograph (Multiple Gas Analyzer #5; SRI Instruments) equipped with a flame ionization detector and a thermal conductivity detector. Ar was used as the carrier gas. Typically, the in-line gas chromatograph was programmed to sample the headspace every 10 min; therefore, the gas products were quantified three times during a 30 min controlled potential electrolysis. The peak areas were converted to gas volumes using a calibration curve created with known concentrations of H_2 and CO. Careful examination of gas chromatography spectra showed the absence of other gas-phase products except H_2 and CO (Supplementary Fig. 6). The Faradaic efficiencies and partial current densities of gas products were reported as the average of three or more independent measurements. Liquid products of electrocatalysis were detected using a Bruker 400 MHz NMR spectrometer. ^{1}H NMR spectra were collected using a water suppression mode (delay time between pulses ($d1$) = 20 s; 32 scans). NMR samples were prepared by adding 450 µl electrolyte taken from the cathode compartment immediately post-electrolysis to an NMR tube containing 50 µl 10.00 mM dimethylmalonic acid (TraceCERT; Sigma–Aldrich) internal standard dissolved in D_2O (99.9 atom%; Sigma–Aldrich). NH_3 was quantified using the indophenol blue method[56] in which NH_3 is converted into indophenol blue via reaction with salicylate and hypochlorite. A series of standard samples with known concentrations of NH_4^+ prepared with NH_4Cl (Macron) were made using the phosphate buffer (0.03 M KH_2PO_4 + 0.035 M K_2HPO_4) + 0.1 M KNO_3 electrolyte and measured to establish the calibration curve based on the maximum absorbance at 652 nm. The NH_3 concentration of an unknown sample was calculated using its absorbance at 652 nm and the calibration curve. A blank sample prepared from fresh electrolyte was measured before every ultraviolet–visible absorption experiment to ensure there was no contamination of the electrolyte and serve as the baseline.

AFM-IR measurement

Samples for AFM and AFM-IR measurements were prepared by solvating 0.1 mg ml^{-1} of the desired solid material followed by sonication. Bare CNTs, CoPc and CoPc–NH_2 aggregates were solvated in DMF, whereas CoPc/CNT and CoPc–NH_2/CNT were solvated in chloroform. The solutions were diluted to 0.01 mg ml^{-1} followed by a second sonication. The dispersed materials were drop-cast on a 15-nm-thick gold film that was evaporated on a silicon wafer. The Au-coated wafer was annealed to 100 °C before drop-casting.

AFM-IR measurements were performed at tapping mode using a nanoIR3 (Bruker) setup equipped with a Bruker hyperspectral quantum cascade laser source (790–1,950 cm^{-1}), gold-coated Si probes with a nominal diameter of ~25 nm, resonance frequencies of 75 ± 15 kHz and spring constants of 1–7 N m^{-1}. The average spectral acquisition time was 5 s per spectrum with a spectral resolution of 2 cm^{-1}.

In situ SFG measurement

The SFG system has been described previously[33,34]. In brief, it uses a Ti:sapphire regenerative amplifier (Solstice; Spectra-Physics) that outputs 90 fs pulses at 800 nm with an average power of 3.5 W. 70% of the output is used to pump an optical parametric amplifier (TOPAS Prime) and generates the infrared beam. The remaining 30% visible beam is spectrally narrowed to 10 cm^{-1} using an air gap etalon (TecOptics). Both infrared and visible beams are incident on the homemade SFG cell in a Kretschmann configuration. The visible beam is delayed for ~700 fs relative to the infrared beam to suppress the non-resonant signal. To make the electrode for SFG measurement, a 50 nm Ag thin film is first deposited on the CaF_2 window through electron beam physical vapour deposition (DV-502A E-Gun Evaporator; Denton), followed by another 2.5 nm ultrathin Al_2O_3 passivation layer deposited by atomic layer deposition (Picosun SUNALE R-150B). The catalysts are then drop-cast on the electrode surface using the same protocol and loading as the kinetics measurement, as stated above. The electrolyte is made from purging CO_2 (99.999%; Praxair) into 0.05 M K_2CO_3 (99.995%; Sigma–Aldrich) or Li_2CO_3 (99.997%; Sigma–Aldrich) dissolved in ultra-pure Milli-Q water for 30 min, which completely converts it into $KHCO_3$ (or $LiHCO_3$). A BioLogic SP-50 potentiostat is employed to apply the potential to the electrode during the in situ SFG measurement. For crown ether, a stoichiometric amount of 18-Crown-6 (>99%; Sigma–Aldrich) is added to $KHCO_3$ to obtain a concentration of 0.1 M. An Au mesh (99.999%; Thermo Fisher Scientific) is used as the counter electrode and a Nafion membrane is used to separate the cathode and anode compartments.

DFT calculation

DFT calculations were performed with Gaussian 16 revision A.03 (ref. 57) using the unrestricted Tao, Perdew, Staroverov and Scuseria level of theory with D3 corrections (Becke–Johnson damping)[58,59] in solution (water; $\varepsilon = 78.3553$) via the solvation model based on density approach[60]. Geometry optimizations were run with the def2-TZVP basis set for Co and the def2-SVP basis set for all other atoms (denoted BS1)[61,62]. Additional single-point calculations for electronic energy refinement purposes were run in solution using the def2-TZVPP basis set for all atoms (denoted BS2). The integration grid was specified to 99 radial shells around each atom, with 590 angular points per shell. Stability analyses were performed in addition to analytical frequency calculations on all stationary points to ensure that geometries corresponded to local minima (all positive eigenvalues) or the transition state (one negative eigenvalue). Intrinsic reaction coordinate calculations and subsequent geometry optimizations were used to confirm the minima linked by each transition state[63,64]. Although the initial computed energies output by Gaussian are given in the gas phase at 1 atm and 298.15 K, all of the reported free energies in this paper were converted to the condition for solution phase at 1 M and 298.15 K by adding 1.89 kcal mol^{-1} to the free energies using the equation $\Delta G^{\rightarrow *} = RT\ \ln[24.4654]$, where R is the ideal gas constant and T is the temperature of the reaction. The GoodVibes program was used to implement this conversion, along with quasi-harmonic oscillator corrections to entropic contributions implemented by Grimme[65] and Head–Gordon's quasi-harmonic approach to enthalpy[66]. A variety of DFT functionals were employed to benchmark the C–O bond stretching frequency ν_{CO} of the CoPc–CO adduct, $(\mathbf{I1})^-$, with and without explicit water, and the results are reported in the Supplementary Information. Additional details of DFT calculations are provided in the Supplementary Methods, Supplementary Figs. 21–24 and Supplementary Tables 1–15.

Data availability

All of the experimental data supporting the findings of this study are available within the supplementary materials. Source data are provided with this paper.

References

1. Corbin, N., Zeng, J., Williams, K. & Manthiram, K. Heterogeneous molecular catalysts for electrocatalytic CO_2 reduction. *Nano Res.* **12**, 2093–2125 (2019).
2. Wu, Y., Liang, Y. & Wang, H. Heterogeneous molecular catalysts of metal phthalocyanines for electrochemical CO_2 reduction reactions. *Acc. Chem. Res.* **54**, 3149–3159 (2021).
3. Wu, X. et al. Molecularly dispersed cobalt phthalocyanine mediates selective and durable CO_2 reduction in a membrane flow cell. *Adv. Funct. Mater.* **32**, 2107301 (2022).
4. Wang, M. et al. CO_2 electrochemical catalytic reduction with a highly active cobalt phthalocyanine. *Nat. Commun.* **10**, 3602 (2019).
5. Zhang, X. et al. Molecular engineering of dispersed nickel phthalocyanines on carbon nanotubes for selective CO_2 reduction. *Nat. Energy* **5**, 684–692 (2020).
6. Sun, C. et al. Three-dimensional graphene-supported cobalt phthalocyanine as advanced electrocatalysts for oxygen reduction reaction. *J. Electrochem. Soc.* **165**, F24 (2018).
7. Chen, R., Li, H., Chu, D. & Wang, G. Unraveling oxygen reduction reaction mechanisms on carbon-supported Fe-phthalocyanine and Co-phthalocyanine catalysts in alkaline solutions. *J. Phys. Chem. C* **113**, 20689–20697 (2009).
8. Wu, Y., Jiang, Z., Lin, Z., Liang, Y. & Wang, H. Direct electrosynthesis of methylamine from carbon dioxide and nitrate. *Nat. Sustain.* **4**, 725–730 (2021).
9. Chebotareva, N. & Nyokong, T. Metallophthalocyanine catalysed electroreduction of nitrate and nitrite ions in alkaline media. *J. Appl. Electrochem.* **27**, 975–981 (1997).
10. Lieber, C. M. & Lewis, N. S. Catalytic reduction of carbon dioxide at carbon electrodes modified with cobalt phthalocyanine. *J. Am. Chem. Soc.* **106**, 5033–5034 (1984).
11. Zhang, X. et al. Highly selective and active CO_2 reduction electrocatalysts based on cobalt phthalocyanine/carbon nanotube hybrid structures. *Nat. Commun.* **8**, 14675 (2017).
12. Lu, X. et al. High-performance electrochemical CO_2 reduction cells based on non-noble metal catalysts. *ACS Energy Lett.* **3**, 2527–2532 (2018).
13. Wu, Y., Jiang, Z., Lu, X., Liang, Y. & Wang, H. Domino electroreduction of CO_2 to methanol on a molecular catalyst. *Nature* **575**, 639–642 (2019).
14. Li, N., Lu, W., Pei, K. & Chen, W. Interfacial peroxidase-like catalytic activity of surface-immobilized cobalt phthalocyanine on multiwall carbon nanotubes. *RSC Adv.* **5**, 9374–9380 (2015).
15. Swarbrick, J. C., Weng, T.-C., Schulte, K., Khlobystov, A. N. & Glatzel, P. Electronic structure changes in cobalt phthalocyanine due to nanotube encapsulation probed using resonant inelastic X-ray scattering. *Phys. Chem. Chem. Phys.* **12**, 9693–9699 (2010).
16. Su, J. et al. Strain enhances the activity of molecular electrocatalysts via carbon nanotube supports. *Nat. Catal.* **6**, 818–828 (2023).
17. Vijay, S. et al. Unified mechanistic understanding of CO_2 reduction to CO on transition metal and single atom catalysts. *Nat. Catal.* **4**, 1024–1031 (2021).
18. Li, H. et al. Stimulating the pre-catalyst redox reaction and the proton–electron transfer process of cobalt phthalocyanine for CO_2 electroreduction. *J. Phys. Chem. C* **126**, 9665–9672 (2022).
19. Zhang, Z. et al. Reaction mechanisms of well-defined metal–N_4 sites in electrocatalytic CO_2 reduction. *Angew. Chem. Int. Ed.* **57**, 16339–16342 (2018).
20. Chang, Q. et al. Metal-coordinated phthalocyanines as platform molecules for understanding isolated metal sites in the electrochemical reduction of CO_2. *J. Am. Chem. Soc.* **144**, 16131–16138 (2022).
21. Zeng, J. S., Corbin, N., Williams, K. & Manthiram, K. Kinetic analysis on the role of bicarbonate in carbon dioxide electroreduction at immobilized cobalt phthalocyanine. *ACS Catal.* **10**, 4326–4336 (2020).
22. Wang, X. et al. In situ scanning tunneling microscopy of cobalt-phthalocyanine-catalyzed CO_2 reduction reaction. *Angew. Chem. Int. Ed.* **59**, 16098–16103 (2020).
23. Xia, Y. et al. Identification of dual-active sites in cobalt phthalocyanine for electrochemical carbon dioxide reduction. *Nano Energy* **67**, 104163 (2020).
24. Zhu, M., Ye, R., Jin, K., Lazouski, N. & Manthiram, K. Elucidating the reactivity and mechanism of CO_2 electroreduction at highly dispersed cobalt phthalocyanine. *ACS Energy Lett.* **3**, 1381–1386 (2018).
25. Chen, X., Wei, D. & Ahlquist, M. S. Aggregation and significant difference in reactivity therein: blocking the CO_2-to-CH_3OH reaction. *Organometallics* **40**, 3087–3093 (2021).
26. Shi, L.-L., Li, M., You, B. & Liao, R.-Z. Theoretical study on the electro-reduction of carbon dioxide to methanol catalyzed by cobalt phthalocyanine. *Inorg. Chem.* **61**, 16549–16564 (2022).
27. Ren, X. et al. In-situ spectroscopic probe of the intrinsic structure feature of single-atom center in electrochemical CO/CO_2 reduction to methanol. *Nat. Commun.* **14**, 3401 (2023).
28. Dery, S., Friedman, B., Shema, H. & Gross, E. Mechanistic insights gained by high spatial resolution reactivity mapping of homogeneous and heterogeneous (electro) catalysts. *Chem. Rev.* **123**, 6003–6038 (2023).
29. Gross, E. Challenges and opportunities in IR nanospectroscopy measurements of energy materials. *Nano Res.* **12**, 2200–2210 (2019).
30. Hermansson, K. Blue-shifting hydrogen bonds. *J. Phys. Chem. A* **106**, 4695–4702 (2002).
31. Tamami, M., Zhang, K., Dixit, N., Moore, R. B. & Long, T. E. Association of nucleobase-containing ammonium ionenes. *Macromol. Chem. Phys.* **215**, 2337–2344 (2014).
32. Wallentine, S., Bandaranayake, S., Biswas, S. & Baker, L. R. Direct observation of carbon dioxide electroreduction on gold: site blocking by the stern layer controls CO_2 adsorption kinetics. *J. Phys. Chem. Lett.* **11**, 8307–8313 (2020).
33. Zhu, Q., Wallentine, S. K., Deng, G.-H., Rebstock, J. A. & Baker, L. R. The solvation-induced onsager reaction field rather than the double-layer field controls CO_2 reduction on gold. *JACS Au* **2**, 472–482 (2022).
34. Wallentine, S., Bandaranayake, S., Biswas, S. & Baker, L. R. Plasmon-resonant vibrational sum frequency generation of electrochemical interfaces: direct observation of carbon dioxide electroreduction on gold. *J. Phys. Chem. A* **124**, 8057–8064 (2020).
35. Huo, S.-J., Wang, J.-Y., Sun, D.-L. & Cai, W.-B. Attenuated total reflection surface-enhanced infrared absorption spectroscopy at a cobalt electrode. *Appl. Spectrosc.* **63**, 1162–1167 (2009).
36. Bradshaw, A. M. & Pritchard, J. Infrared spectra of carbon monoxide chemisorbed on metal films: a comparative study of copper, silver, gold, iron, cobalt and nickel. *Proc. R. Soc. Lond. Ser. A* **316**, 169–183 (1970).
37. Bhattacharyya, D. et al. Sub-nanometer mapping of the interfacial electric field profile using a vibrational Stark shift ruler. *J. Am. Chem. Soc.* **144**, 14330–14338 (2022).

38. Kutzler, F. W., Barger, W. R., Snow, A. W. & Wohltjen, H. An investigation of conductivity in metal-substituted phthalocyanine Langmuir–Blodgett films. *Thin Solid Films* **155**, 1–16 (1987).
39. Shihub, S. & Gould, R. Frequency dependence of electronic conduction parameters in evaporated thin films of cobalt phthalocyanine. *Thin Solid Films* **254**, 187–193 (1995).
40. Ren, S. et al. Catalyst aggregation matters for immobilized molecular CO_2RR electrocatalysts. *J. Am. Chem. Soc.* **145**, 4414–4420 (2023).
41. Wang, Y.-Q. et al. Probing the synergistic effects of Mg^{2+} on CO_2 reduction reaction on CoPc by in situ electrochemical scanning tunneling microscopy. *J. Am. Chem. Soc.* **144**, 20126–20133 (2022).
42. Li, P. et al. Hydrogen bond network connectivity in the electric double layer dominates the kinetic pH effect in hydrogen electrocatalysis on Pt. *Nat. Catal.* **5**, 900–911 (2022).
43. Franzen, S. An electrostatic model for the frequency shifts in the carbonmonoxy stretching band of myoglobin: correlation of hydrogen bonding and the Stark tuning rate. *J. Am. Chem. Soc.* **124**, 13271–13281 (2002).
44. Ovalle, V. J., Hsu, Y.-S., Agrawal, N., Janik, M. J. & Waegele, M. M. Correlating hydration free energy and specific adsorption of alkali metal cations during CO_2 electroreduction on Au. *Nat. Catal.* **5**, 624–632 (2022).
45. Monteiro, M. C. et al. Absence of CO_2 electroreduction on copper, gold and silver electrodes without metal cations in solution. *Nat. Catal.* **4**, 654–662 (2021).
46. Huang, J. E. et al. CO_2 electrolysis to multicarbon products in strong acid. *Science* **372**, 1074–1078 (2021).
47. Rooney, C. L. et al. Active sites of cobalt phthalocyanine in electrocatalytic CO_2 reduction to methanol. *Angew. Chem.* **136**, e202310623 (2024).
48. Li, X. & Panetier, J. A. Computational study for CO_2-to-CO conversion over proton reduction using [Re[bpyMe(Im-R)] $(CO)_3Cl]^+$ (R=Me, Me_2, and Me_4) electrocatalysts and comparison with manganese analogues. *ACS Catal.* **11**, 12989–13000 (2021).
49. Boutin, E. et al. Aqueous electrochemical reduction of carbon dioxide and carbon monoxide into methanol with cobalt phthalocyanine. *Angew. Chem. Int. Ed.* **58**, 16172–16176 (2019).
50. Li, J. et al. Mechanism-guided realization of selective carbon monoxide electroreduction to methanol. *Nat. Synth.* **2**, 1194–1201 (2023).
51. Salles, F. et al. Hydration sequence of swelling clays: evolutions of specific surface area and hydration energy. *J. Colloid Interface Sci.* **333**, 510–522 (2009).
52. Darwish, I. A. & Uchegbu, I. F. The evaluation of crown ether based niosomes as cation containing and cation sensitive drug delivery systems. *Int. J. Pharm.* **159**, 207–213 (1997).
53. Lehn, J.-M. Supramolecular chemistry-scope and perspectives molecules, supermolecules, and molecular devices (nobel lecture). *Angew. Chem. Int. Ed. Engl.* **27**, 89–112 (1988).
54. Lu, H.-H. et al. Creating a pseudometallic state of K^+ by intercalation into 18-crown-6 grafted on polyfluorene as electron injection layer for high performance pleds with oxygen- and moisture-stable Al cathode. *J. Am. Chem. Soc.* **133**, 9634–9637 (2011).
55. Yang, S. et al. Codeposition modification of cation exchange membranes with dopamine and crown ether to achieve high K^+ electrodialysis selectivity. *ACS Appl. Mater. Interfaces* **11**, 17730–17741 (2019).
56. Wu, Z.-Y. et al. Electrochemical ammonia synthesis via nitrate reduction on Fe single atom catalyst. *Nat. Commun.* **12**, 2870 (2021).
57. Frisch, M. J. et al. Gaussian 16 revision A.03 (Gaussian, 2016).
58. Staroverov, V. N., Scuseria, G. E., Tao, J. & Perdew, J. P. Comparative assessment of a new nonempirical density functional: molecules and hydrogen-bonded complexes. *J. Chem. Phys.* **119**, 12129–12137 (2003).
59. Grimme, S., Ehrlich, S. & Goerigk, L. Effect of the damping function in dispersion corrected density functional theory. *J. Comput. Chem.* **32**, 1456–1465 (2011).
60. Marenich, A. V., Cramer, C. J. & Truhlar, D. G. Universal solvation model based on solute electron density and on a continuum model of the solvent defined by the bulk dielectric constant and atomic surface tensions. *J. Phys. Chem. B* **113**, 6378–6396 (2009).
61. Weigend, F. & Ahlrichs, R. Balanced basis sets of split valence, triple zeta valence and quadruple zeta valence quality for H to Rn: design and assessment of accuracy. *Phys. Chem. Chem. Phys.* **7**, 3297–3305 (2005).
62. Weigend, F. Accurate Coulomb-fitting basis sets for H to Rn. *Phys. Chem. Chem. Phys.* **8**, 1057–1065 (2006).
63. Gonzalez, C. & Schlegel, H. B. An improved algorithm for reaction path following. *J. Chem. Phys.* **90**, 2154–2161 (1989).
64. Gonzalez, C. & Schlegel, H. B. Reaction path following in mass-weighted internal coordinates. *J. Phys. Chem.* **94**, 5523–5527 (1990).
65. Grimme, S. Supramolecular binding thermodynamics by dispersion-corrected density functional theory. *Chem. Eur. J.* **18**, 9955–9964 (2012).
66. Li, Y.-P., Gomes, J., Mallikarjun Sharada, S., Bell, A. T. & Head-Gordon, M. Improved force-field parameters for QM/MM simulations of the energies of adsorption for molecules in zeolites and a free rotor correction to the rigid rotor harmonic oscillator model for adsorption enthalpies. *J. Phys. Chem. C* **119**, 1840–1850 (2015).

Acknowledgements

This work was supported by the United States National Science Foundation (NSF)–United States–Israel Binational Science Foundation (BSF) International Collaboration programme in the Division of Chemical, Bioengineering, Environmental, and Transport Systems (NSF grant number 2129963 and BSF grant number 2021671). The catalyst preparation, kinetic studies and SFG measurements were supported by grant number 2129963 (to Q.Z., C.L.R., H.W. and L.R.B.) from the NSF. The AFM and AFM-IR measurements were supported by grant number 2021671 (to H.S. and E.G.) from the BSF. The DFT calculations were supported by grant number 2154724 (to C.Z. and J.A.P.) from the NSF. We also thank the Spiedie cluster at Binghamton University for performing electronic structure calculations.

Author contributions

C.L.R. prepared the catalysts and conducted the electrocatalytic tests. Q.Z. conducted the SFG measurements. H.S. conducted the AFM-IR measurements. C.Z. performed the DFT calculations. Q.Z., C.L.R., H.S. and C.Z. analysed the results and participated in writing the manuscript. All authors reviewed the manuscript.

Competing interests

The authors declare no competing interests.

Additional information

Supplementary information The online version contains supplementary material available at https://doi.org/10.1038/s41929-024-01190-9.

Correspondence and requests for materials should be addressed to Julien A. Panetier, Elad Gross, Hailiang Wang or L. Robert Baker.

Peer review information *Nature Catalysis* thanks Julien Bonin, Ali Seifitokaldani and the other, anonymous, reviewer(s) for their contribution to the peer review of this work.

Terms and Conditions

Springer Nature journal content, brought to you courtesy of Springer Nature Customer Service Center GmbH (“Springer Nature”).
Springer Nature supports a reasonable amount of sharing of research papers by authors, subscribers and authorised users (“Users”), for small-scale personal, non-commercial use provided that all copyright, trade and service marks and other proprietary notices are maintained. By accessing, sharing, receiving or otherwise using the Springer Nature journal content you agree to these terms of use (“Terms”). For these purposes, Springer Nature considers academic use (by researchers and students) to be non-commercial.
These Terms are supplementary and will apply in addition to any applicable website terms and conditions, a relevant site licence or a personal subscription. These Terms will prevail over any conflict or ambiguity with regards to the relevant terms, a site licence or a personal subscription (to the extent of the conflict or ambiguity only). For Creative Commons-licensed articles, the terms of the Creative Commons license used will apply.
We collect and use personal data to provide access to the Springer Nature journal content. We may also use these personal data internally within ResearchGate and Springer Nature and as agreed share it, in an anonymised way, for purposes of tracking, analysis and reporting. We will not otherwise disclose your personal data outside the ResearchGate or the Springer Nature group of companies unless we have your permission as detailed in the Privacy Policy.
While Users may use the Springer Nature journal content for small scale, personal non-commercial use, it is important to note that Users may not:

1. use such content for the purpose of providing other users with access on a regular or large scale basis or as a means to circumvent access control;
2. use such content where to do so would be considered a criminal or statutory offence in any jurisdiction, or gives rise to civil liability, or is otherwise unlawful;
3. falsely or misleadingly imply or suggest endorsement, approval , sponsorship, or association unless explicitly agreed to by Springer Nature in writing;
4. use bots or other automated methods to access the content or redirect messages
5. override any security feature or exclusionary protocol; or
6. share the content in order to create substitute for Springer Nature products or services or a systematic database of Springer Nature journal content.

In line with the restriction against commercial use, Springer Nature does not permit the creation of a product or service that creates revenue, royalties, rent or income from our content or its inclusion as part of a paid for service or for other commercial gain. Springer Nature journal content cannot be used for inter-library loans and librarians may not upload Springer Nature journal content on a large scale into their, or any other, institutional repository.
These terms of use are reviewed regularly and may be amended at any time. Springer Nature is not obligated to publish any information or content on this website and may remove it or features or functionality at our sole discretion, at any time with or without notice. Springer Nature may revoke this licence to you at any time and remove access to any copies of the Springer Nature journal content which have been saved.
To the fullest extent permitted by law, Springer Nature makes no warranties, representations or guarantees to Users, either express or implied with respect to the Springer nature journal content and all parties disclaim and waive any implied warranties or warranties imposed by law, including merchantability or fitness for any particular purpose.
Please note that these rights do not automatically extend to content, data or other material published by Springer Nature that may be licensed from third parties.
If you would like to use or distribute our Springer Nature journal content to a wider audience or on a regular basis or in any other manner not expressly permitted by these Terms, please contact Springer Nature at

onlineservice@springernature.com